Quenched Slonczewski windmill in spin-torque vortex oscillators

V. Sluka,[1,*] A. Kákay,[1] A. M. Deac,[2] D. E. Bürgler,[1] R. Hertel,[3] and C. M. Schneider[1]

[1]*Peter Grünberg Institute, Electronic Properties (PGI-6) and Jülich-Aachen Research Alliance, Fundamentals of Future Information Technology (JARA-FIT), Forschungszentrum Jülich GmbH, D-52425 Jülich, Germany*

[2]*Institute of Ion Beam Physics and Materials Research, Helmholtz-Zentrum Dresden-Rossendorf e. V., D-01314 Dresden, Germany*

[3]*Institut de Physique et Chimie des Matériaux de Strasbourg, Université de Strasbourg, CNRS UMR 7504, F-67034 Strasbourg Cedex 2, France*

We present a combined analytical and numerical study on double-vortex spin-torque nano-oscillators and describe a mechanism that suppresses the windmill modes. The magnetization dynamics is dominated by the gyrotropic precession of the vortex in one of the ferromagnetic layers. In the other layer, the vortex gyration is strongly damped. The dominating layer for the magnetization dynamics is determined by the sign of the product between sample current and the chiralities. Measurements on Fe/Ag/Fe nanopillars support these findings. The results open up a new perspective for building high quality-factor spin-torque oscillators operating at selectable, well-separated frequency bands.

I. INTRODUCTION

The advent of spintronics lead to the development of exciting new concepts for nanoscale devices using the spin-degree of freedom of the electron besides its charge property.[1] One particular class of devices under intense study over the past years is that of the spin-torque nanooscillators (STNOs).[2–7] Typical STNOs consist of two single domain ferromagnetic layers separated by a metallic spacer or a tunnel barrier, one with its magnetization fixed (polarizing layer), the other one susceptible to torques (free layer). An electric current traversing the system perpendicular to the layers becomes spin-polarized and exerts torques on the magnetizations,[8–10] leading to magnetization dynamics of the free layer. These excitations are typically in the range of a few gigahertz and can be detected by measuring the time variation of the magnetoresistance (MR). STNOs are thus considered as promising candidates for on-chip microwave sources, a technology ingredient that would allow to greatly advance today's state of the art telecommunication.

Commonly investigated STNOs are based on single-domain nanomagnets. Recently however, vortex oscillators have shifted into focus. The magnetic vortex is the ground state of magnetization in disk-shaped ferromagnets with dimensions between the single and the multidomain regimes. With its magnetization mainly parallel to the disk plane and circulating the disk center, the vortex is basically a closed-flux structure. The only surface charges originate from the vortex core, a tiny region with lateral size in the order of the exchange length, where the exchange interaction forces the magnetization out of the disk plane. A particular vortex state is thus determined by two binary parameters. The counter-clockwise or clockwise sense of rotation of the in-plane magnetization (chirality) and the up or down orientation of the out-of-plane core (polarity). The lowest excitation of the vortex state corresponds to a circular motion of the core around the disk center, the gyrotropic mode, with frequencies typically ranging from a few hundred megahertz to about two gigahertz. The corresponding linewidths can reach well below one megahertz, rendering magnetic vortices high quality

oscillators. In their 2007 paper, Pribiag *et al.* reported the excitation of gyrotropic motion by means of spin-transfer torque,[11] opening up the possibility for vortex-based STNOs. Among the considered vortex oscillators, most configurations involved homogeneously magnetized polarizers.[12–19]

Here, we investigate STNOs containing two stacked magnetic vortices, i.e., a system consisting of two ferromagnetic disks, each in a vortex state and separated by a metallic, nonmagnetic spacer [see Fig. 1(b)]. Such double-vortex systems have so far rarely been treated in the literature,[20] although they actually represent a natural choice. Depending on the relative chiralities, the vortex pair can be either in a parallel or antiparallel configuration, thus constituting the analog of the single-domain case. Besides the choice of vortices instead of homogeneously magnetized layers, there is another fundamental difference between our device and typical STNOs: in our double-vortex system, neither of the two ferromagnets is pinned, that is, one vortex serves as the polarizer for the other and vice versa. Thus, in both layers, magnetization dynamics can be excited by spin-transfer torque. This is a particularly interesting condition, since for the case of two spin-torque-coupled macrospins the spin-transfer torque has the tendency to conserve the relative angle of the two moments. A dynamic state where both macrospins precess while their relative angle remains constant in time is referred to as Slonczewski windmill. It has been shown[21] that in single-domain-based STNOs, such states can appear if the degree of symmetry between the two layers is sufficiently high.

We employ analytical and numerical methods to study the coupled spin-torque-driven motion of the vortices in the two disks. First, we analyze in detail the underlying torques and the resulting force that one vortex exerts onto the other. We then numerically solve the spin-torque-coupled Thiele equations for the two-vortex system. The analysis of the spin-torque-driven dynamics yields an intriguing mechanism that quenches windmill modes. It turns out that the sign of the current-chiralities-product determines which disk is excited and thereby the frequency band at which the device is operating. These theoretical findings are supported by our
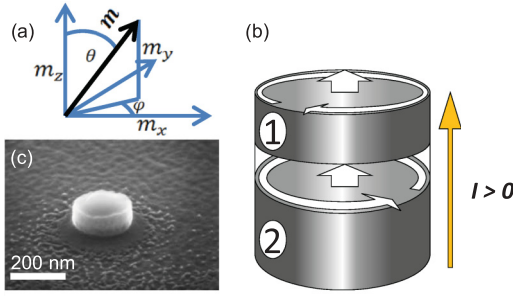
FIG. 1. (Color online) Coordinate system (a) and sample structure (b) used in the calculation. The sample consists of two ferromagnetic disks (1 and 2), each containing a vortex characterized by its chirality and core polarity (illustrated by the white arrows). The two ferromagnetic layers are separated by a metallic, nonmagnetic spacer (transparent). The positive technical current direction is shown, corresponding to an electron flow from the top to the bottom layer. (c) Scanning electron micrograph of a nanocontact after ion beam etching.

experimental data obtained from double-vortex Fe/Ag/Fe STNOs.

II. MODEL

Figure 1(b) depicts the considered sample geometry. The motion of the magnetic vortex in each of the disks is governed by the Thiele equation[22] that we write here for the vortex in the top disk, as indicated by the indices:

$$\mathbf{G}_1 \times \frac{d\mathbf{X}_1}{dt} - \frac{dW_1}{d\mathbf{X}_1} - D_1 \frac{d\mathbf{X}_1}{dt} + \frac{\hbar j P}{4e} \mathbf{F}_1 = 0. \quad (1)$$

$\mathbf{G} = -2\pi\kappa(\mu_0 M_s L/\gamma)\hat{\mathbf{e}}_z$ is the gyro vector, where L and $\kappa = \pm 1$ are the disk thickness and the vortex core polarity, respectively. $\mathbf{X}$ is the core position with respect to the disk center, W refers to the effective magnetostatic potential in which the core is moving, and $D = (\alpha\mu_0 M_s/\gamma)L\pi\ln(R/r_0)$ characterizes the damping of the vortex motion. The parameters R and r_0 are the radii of the disk and the vortex core. An analog equation, with the index 1 replaced by 2 holds for the bottom disk. The term $\mathbf{F}_1$ in Eq. (1) corresponds to the spin-transfer torque-induced force acting on vortex 1. This force is generated by vortex 2 in the bottom disk, which acts as a polarizer for the magnetization in disk 1 (and vice versa). Before we investigate the coupled dynamics of the two vortices, we will first consider the characteristics of the spin-transfer torque-induced force term in more detail.

$\mathbf{F}_1$ can be decomposed into two contributions $\mathbf{F}_1 = \mathbf{F}_1^d + \mathbf{F}_1^c$. $\mathbf{F}_1^d$ arises from the in-plane magnetization of vortex 2 and acts on the core of vortex 1. The second term $\mathbf{F}_1^c$ is caused by the core of the polarizer vortex and acts on the in-plane magnetization of vortex 1. Both force contributions depend on the lateral core-core distance l. Following Ref. 23, we obtain the expressions

$$\mathbf{F}_1^d = \int_A d^2x \, [m_{2,x}\sin(\varphi) - m_{2,y}\cos(\varphi)]\nabla\theta$$
$$+ \sin(\varphi)\cos(\varphi)[m_{2,x}\cos(\varphi) + m_{2,y}\sin(\varphi)]\nabla\varphi$$
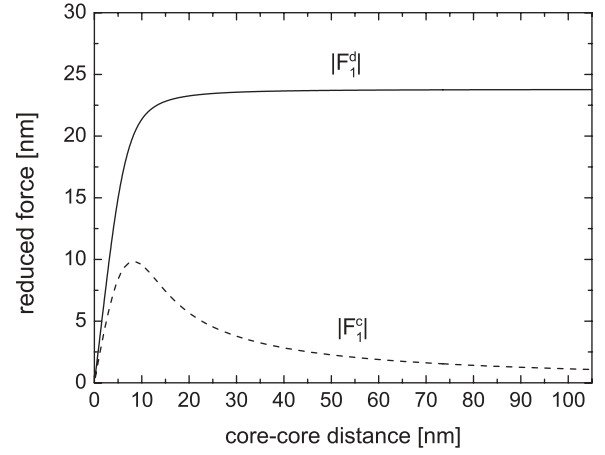$$= C_1 C_2 \kappa_1 F^d \hat{\mathbf{e}}_{12} \quad (2)$$

FIG. 2. Spin-torque magnitudes exerted by disk 2 on the vortex in disk 1 and their dependence on the lateral core-core separation. The torque arising from the polarizer core, F_1^c is negligible at large distances, explaining the results obtained by micromagnetic simulations and presented in Ref. 26.

and

$$\mathbf{F}_1^c = -\int_A d^2x \, m_{2,z}\sin^2(\theta)\nabla\varphi = \kappa_2 F^c \hat{\mathbf{e}}_{12}, \quad (3)$$

where we introduce the vectors

$$\hat{\mathbf{e}}_{12} = -\hat{\mathbf{e}}_{21} = \frac{\hat{\mathbf{e}}_z \times (\mathbf{X}_1 - \mathbf{X}_2)}{\sqrt{(X_1 - X_2)^2 + (Y_1 - Y_2)^2}}. \quad (4)$$

$C_i = \pm 1$ defines the chirality of vortex i ("$+$" corresponds to counterclockwise, "$-$" to clockwise) and $m_{2,j}$ refers to the jth component of the bottom vortex unit magnetization vector. The top layer magnetization is written in spherical coordinates (φ, θ), where φ and θ are the azimuthal and polar angles, respectively. The cylinder axis is chosen as the z axis [see Fig. 1(a)]. In the calculation we assume rigid vortices with z-independent magnetization. Using the ansatz of Feldtkeller and Thomas[24] for the out-of-plane core magnetization ($|m_{i,z}| = \exp(-a^2 r^2)$ with $a^2 \approx \ln 2/(25\text{ nm}^2)$ for the vortex core size in Fe),[25] we obtain the forces and their dependence on the lateral core-core distance l as shown in Fig. 2. For large l, the contribution of $\mathbf{F}_1^c$ to the total force becomes negligible. This is in agreement with the simulation results reported in Ref. 26, where the influence of the polarizer-vortex core on the dynamics was found to be small. From Eq. (3) we see that this is caused by the reduction of the function $|\nabla\varphi|$ with increasing distance from the top vortex core. In contrast to the asymptotic decrease of $\mathbf{F}_1^c$ to zero, the magnitude of $\mathbf{F}_1^d$ approaches a finite value for large l. For small distances $l < 2r_0 \approx 10$ nm, however, we observe that both torques fall to zero. This can be attributed to the gain in symmetry with decreasing core-core distance. The small torque introduced by $\mathbf{F}_1^c$ is neglected in our investigation on the dynamics of the system with the vortices coupled by the electric current. This is justified by the fact that we are interested in the situation when the system is excited to high amplitudes, that is, when large current densities are applied. The decrease of $\mathbf{F}_1^d$ at small l must, however, be included.

The coupled Thiele equations for vortices 1 and 2 read, with $\tilde{j} := \hbar j P/(4e)$

$$\mathbf{G}_1 \times \frac{d\mathbf{X}_1}{dt} - \frac{dW_1}{d\mathbf{X}_1} - D_1 \frac{d\mathbf{X}_1}{dt} + \tilde{j} C_1 C_2 \kappa_1 F^d \hat{\mathbf{e}}_{12} = 0, \quad (5)$$

$$\mathbf{G}_2 \times \frac{d\mathbf{X}_2}{dt} - \frac{dW_2}{d\mathbf{X}_2} - D_2 \frac{d\mathbf{X}_2}{dt} - \tilde{j} C_1 C_2 \kappa_2 F^d \hat{\mathbf{e}}_{21} = 0. \quad (6)$$

The sign of $\tilde{j}$ is positive for electron flow from the top to the bottom layer [see Fig. 1(b)]. The effective magnetostatic potential of a vortex inside a disk consists of several energy terms: the exchange and demagnetizing energies as well as the Zeemann energy of the vortex in the current-induced Oersted field depend on the coordinates of the vortex core and thus lead to an effective energy landscape. Expressions for the latter two contributions are, for instance, given in Refs. 15 and 23. Here, we do not attempt to compute the effective potentials of the vortices. Since the parameters defining the materials and the geometry are fixed quantities, we simply use potentials of parabolic form that yield reasonable gyro-frequencies for each uncoupled disk, i.e., $W_i = k_i \mathbf{X}_i^2$. The proportionality constants k_1 and k_2 define the free-running gyrofrequencies f_1^0 and f_2^0 of disk 1 and disk 2, respectively. For clarity, the Oersted field is neglected at this point. Its effect would be to shift k_i to higher or lower values, depending on whether its chirality is equal or opposite to that of vortex i. For the numerical solution of the spin-torque-coupled Thiele equations, we choose $f_1^0 = 1.0$ GHz and $f_2^0 = 1.67$ GHz as to represent our Fe/Ag/Fe nanopillars. These adjustments are achieved by letting $W_1(\mathbf{X}_1)/|\mathbf{G}_1| = 6.28$ ns$^{-1}\mathbf{X}_1^2/2$ and $W_2/|\mathbf{G}_2| = (5/3)W_1/|\mathbf{G}_1|$. The factor of 5/3 thereby corresponds to the thickness ratio of the ferromagnetic disks in our nanopillar and accounts for the fact that the gyrofrequency of a ferromagnetic disk roughly scales with the disk aspect ratio.[27] Furthermore, we use a current of $\tilde{j}/|\mathbf{G}_1| = (5/23)$ ns^{-1} corresponding to about 1.12×10^{12} A/m^2 (for $P = 1$), which is within the range of experiments. The spin-transfer torque-induced force F^d is assumed to increase linearly from $l = 0$ to 10 nm, from whereon it is set to the constant value $F_\infty^d = 23$ nm.

The solutions to Eqs. (5) and (6) are obtained numerically using MAPLE's rkf45 implementation.[28] The results can be summarized as follows: for positive currents and equal chiralities, the top vortex gyrates around the disk center on a trajectory of about 50 nm in radius, regardless of the core polarity. The sense of rotation is determined by the core polarization (counterclockwise for positive and clockwise for negative core polarity). The gyration frequency is 1.0 GHz. The bottom vortex adapts its frequency and sense of gyration according to the top vortex. A dynamic equilibrium develops with a constant phase difference between the vortices even in the case of opposite relative core orientation. This frequency adaption is accompanied by a strong reduction in radius of the bottom core trajectory: for parallel cores, the radius is about 0.7 nm, while for the antiparallel configuration, the reduction is even more pronounced (approximately 0.2 nm). For negative currents, the vortices switch roles: the bottom vortex gyrates on a large orbit (18 nm), while the top vortex trajectory is quenched (1.2 nm for parallel, 0.3 nm for antiparallel core alignment). In the dynamic equilibrium the phase difference is constant
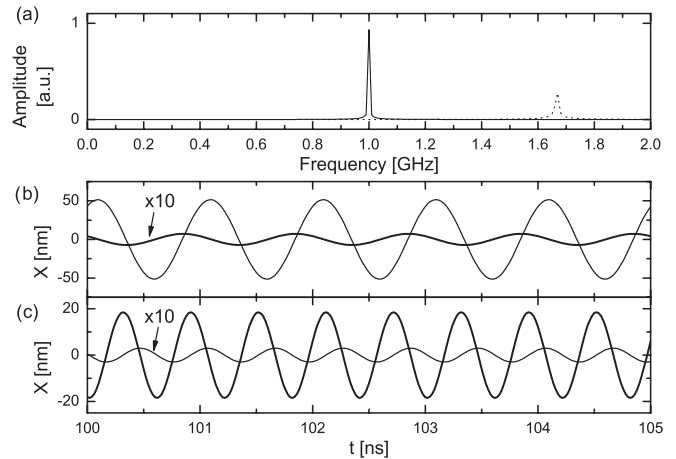

FIG. 3. Vortex dynamics obtained for the case of equal chiralities, represented by the time variation of the respective X coordinates of the vortex cores. (a) For positive and negative current, the system gyrates at 1.0 GHz (solid) and 1.67 GHz (dotted), respectively. The X coordinate of the vortex cores is shown in the lower panels for positive (b) and negative (c) currents. The thin line corresponds to the top, the thick line to the bottom vortex. In (b), both cores have positive polarity, while in (c) they are antiparallel with the bottom core pointing down.

and the gyration frequency is about 1.67 GHz. This frequency corresponds to the eigenfrequency of the bottom vortex while the sense of rotation is determined by its core polarity. The gyration phase difference between the two vortices depends on the relative core alignment. For positive currents and equal chiralities, the bottom core gyrates approximately $\pi/2$ ahead of its top counterpart if the cores are parallel, while for antiparallel cores a $-\pi/2$ lag is observed. Figures 3(b) and 3(c) depict the X coordinates of the two vortex cores for positive and negative current, respectively. Figure 3(a) displays the resulting spectra, in each case obtained from the dynamics in the dominantly excited disk. From Eqs. (5) and (6), it is clear that the solutions for opposite chiralities are identical to those obtained for equal chiralities with a negative current polarity.

For large enough $|j|$, the obtained characteristics of the dynamics are the generalization of the criterion found in Ref. 26. In the model used by those authors, the polarizer was assumed to be a fixed, rigid vortex, and only magnetization dynamics in the other, free disk was allowed. In our case, both disks can be polarizing or free layer. For a given combination of chiralities $C_1 C_2$ and applied current polarity, the system responds with a damped and a dominant gyration, the former defining the polarizing and the latter the free disk. As is evident from Eqs. (5) and (6), it is the product of current and chiralities that matters. For given chiralities, the current polarity determines which disk is dominantly excited. On the other hand, changing the current sign influences the dynamics in the same way as changing one of the chiralities. Therefore we can write down a generalized jCC criterion: for $jC_1 C_2 > 0$ the top and for $jC_1 C_2 < 0$, the bottom disk is excited.

A general analytical solution for steady state trajectories is difficult to establish due to the complexity of the denominator in Eq. (4); however, it is instructive to analyze the situation

when one trajectory radius is much larger than the other, a condition that, according to our numerical results, also holds in the vicinity of the limit cycle. We define $r_i := \sqrt{X_i^2 + Y_i^2}$ and consider the case of positive jC_1C_2. Requiring that the whole system gyrates at a frequency f while the bottom vortex has a phase ϕ with the top vortex we find, up to first order in r_2/r_1, the following relations:

$$
\begin{aligned}
&r_2(\phi) \\
&= \left[\frac{|\mathbf{G}_2|}{D_2} \cos(\phi) + \kappa_2 \sin(\phi) \right] \\
&\times \left\{ \frac{2\pi \kappa_2 |\mathbf{G}_2| f_2^0}{\tilde{j} C_1 C_2 F_\infty^d} - \frac{\sin(\phi)}{r_1} \left[\kappa_2 \cos(\phi) - \frac{|\mathbf{G}_2|}{D_2} \sin(\phi) \right] \right\}^{-1},
\end{aligned}
\tag{7}
$$

$$
f(\phi) = \frac{\tilde{j} C_1 C_2 F_\infty^d \kappa_2}{2\pi D_2} \left[\frac{\cos(\phi)}{r_2(\phi)} - \frac{\sin^2(\phi)}{r_1} \right].
\tag{8}
$$

These relations are displayed in Fig. 4 in the limit $r_2/r_1 \to 0$ and reproduce the behavior observed in the numerical solutions: for both cases of positive [see Fig. 4(b)] and negative [see Fig. 4(c)] bottom vortex core polarity, the bottom vortex can adapt to the (*a priori* arbitrary) frequency of the top vortex by adjusting the phase. Positive (negative) frequency corresponds to counterclockwise (clockwise) gyration. As displayed in Fig. 4(a), this phase shifting is accompanied by a strong reduction of the orbit radius or, in other words, a quenching of the windmill modes. By means of a phase adaption and reduction of the radius, the vortex can use a fraction of the spin-transfer torque-induced force to assist or counteract the force due to its magnetostatic potential. The resulting radial force component can differ strongly from the purely magnetostatic force. It may even lead to an inversion of the relation between the sense of gyration and the core polarity. The closer the eigenfrequencies of the two disks are to each other, the lesser is the need for frequency adaption, given that the vortices exhibit equal polarities. As a consequence, the distance between the moving vortices decreases for a given
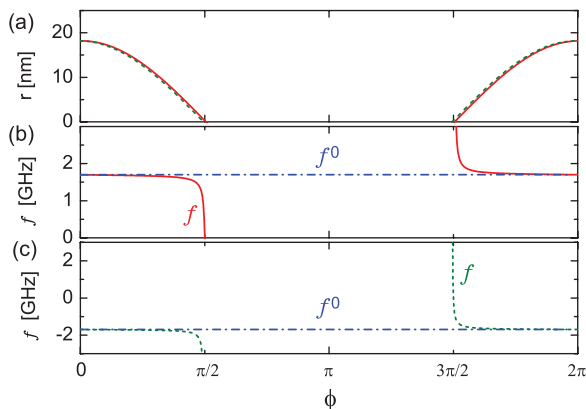

FIG. 4. (Color online) Trajectory radius r (a) and frequency f [(b) and (c)] of the bottom vortex as functions of the phase ϕ with respect to the top vortex which gyrates at the same frequency. The solid and dashed lines correspond to positive and negative bottom vortex core polarity, respectively. The dash-dotted lines mark the eigenfrequency f^0 of the uncoupled bottom vortex for positive (b) and negative (c) core polarity.
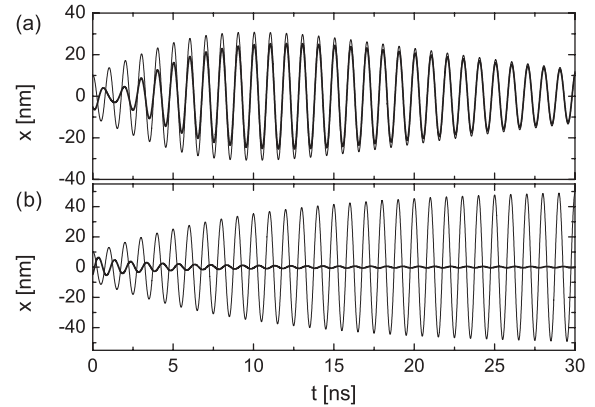

FIG. 5. X components of the top (thin line) and bottom (thick line) core coordinates versus time for the case of symmetric disks. The cores are aligned parallel in (a) and antiparallel in (b). In the parallel case, a windmill mode only appears in a transient time interval, but is hindered afterwards. The oscillation decays due to the low core separation and the related decrease of the spin-transfer torque-induced force.

current, as one eigenfrequency approaches the other. If the intercore distance falls below the core diameter, the mutual spin-torque-induced force decreases, too. Figure 5(a) displays the extreme case, where the two disks are identical and the cores parallel. In this configuration, the vortices start rotating in phase, but as they reach the limit cycle and the core-core distance drops below 10 nm, the mutual spin-transfer torque-induced force decreases, leading to a decay of the oscillation amplitudes. For antiparallel alignment, the windmill modes are quenched by the mechanism of frequency and phase adaption [see Fig. 5(b)].

III. EXPERIMENT

In order to check the validity of our theoretical model we study the current-induced magnetization dynamics of an Fe/Ag/Fe nanopillar with a Fe layer thickness ratio of 5/3. According to the model, we expect to observe excitations for both current polarities, but with different frequencies yielding a frequency ratio of approximately 5/3. Cylindrical nanopillars are patterned using e-beam lithography and Ar ion milling from molecular beam epitaxy-grown GaAs(001)/Fe(1)/Ag(150)/Fe(25)/Ag(6)/Fe(15)/Au(25) stacks [layer thicknesses in nm, see Fig. 1(c) for a scanning electron microscopy (SEM) image]. SEM yields a pillar diameter of about 210 nm. The milling was stopped after reaching the 150-nm-thick Ag buffer layer. Thus the oscillator consists of two ferromagnetic disks of equal diameter and comparable thickness stacked on top of each other. Figures 6(d)–6(f) display the field dependence of the nanopillar resistance for $I = +21$ mA [(d) and (f)] and $I = -21$ mA (e), corresponding to a current density of $\pm 6.1 \times 10^7$ A/cm^2, respectively. The external magnetic field is applied in the sample plane with the field sweep direction from negative to positive in Figs. 6(a) and 6(d) and in the opposite direction for Figs. 6(b), 6(c), 6(e), and 6(f). The magnetoresistance profiles are characteristic for this sample type[29] and reflect two magnetization states: the first one
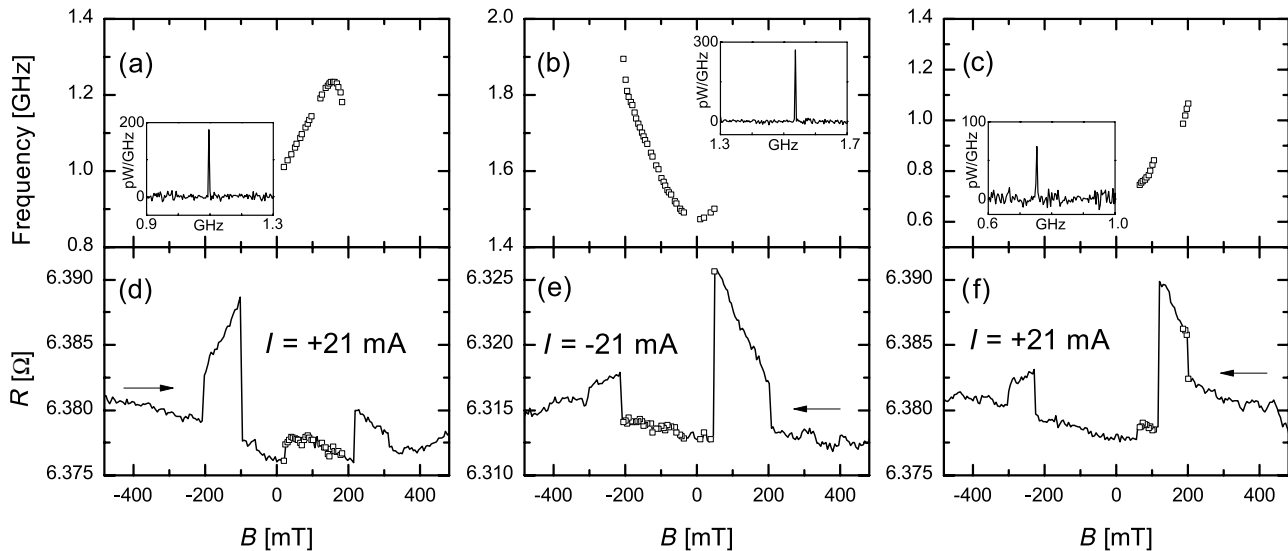
FIG. 6. Resistance vs field measurements at sample currents of $+21$ mA [(d) and (f)] and for -21 mA (e). Simultaneously to the resistance measurements, the high-frequency spectra resulting from the magnetization dynamics were recorded. The square symbols on the MR curves indicate data points at which the corresponding spectrum displayed a peak (regardless of whether or not the sample was in a double vortex state). The top panels (a)–(c) display the peak frequencies. The insets to (a)–(c) show single spectra recorded at a field magnitude of about 70 mT. Arrows indicate the sweep directions. The second sweep belonging to negative current is not shown, since no magnetization dynamics was visible in the double vortex state.

comprises a vortex in one disk, while the other nanomagnet remains in a quasihomogeneous state. These configurations are characterized by a nearly linear field dependence of the resistance [e.g., Fig. 6(d) between -200 and -100 mT] caused by a continuous lateral displacement of the vortex with changing field. The second state is observed from low-field magnitudes up to about 200 mT and is characterized by low resistance values near the level in magnetic saturation. Here, each disk contains a vortex with the chirality given by the circumferential Oersted field. This results in locally parallel alignment of the two disks' magnetizations explaining the observed low resistance. Simultaneously to the dc measurements we recorded the high-frequency spectra, thus allowing to correlate the information about magnetization dynamics with the magnetoresistance curve. Figures 6(a)–6(c) display the peak frequencies from the spectra corresponding to the field sweeps in Figs. 6(d)–6(f), respectively. The insets to Figs. 6(a)–6(c) show sample spectra measured at a field magnitude of 70 mT. As is apparent from Fig. 6, for both current polarities we detected magnetization dynamics in those field intervals, in which the double-vortex state occurs. The excitation frequencies are below 2 GHz, which is typical for vortex gyration in Fe/Ag/Fe nanopillars,[16,29,30] but the frequencies are clearly different and well separated for the two current polarities. If we compare the modes shown in Figs. 6(a) and 6(b) at low external fields, their ratio is about 1.46. Using previous data on single vortex dynamics,[15,29] we estimate the influence of the Oersted field on the zero-field vortex frequencies to be about 145 MHz for both disks. This shifts the above value to 1.54, i.e., very close to the ratio of the disk aspect ratios ($5/3 \simeq 1.67$), which is the value predicted by our model. One should bear in mind, however, that in Eqs. (5) and (6), the dipolar interaction between the vortices has been neglected. This interaction is expected to

influence the modes and their respective frequencies in real samples. The dipolar interaction between the vortices may vary from sweep to sweep, e.g., when configurations with different core polarization alignments nucleate after reducing the field from saturation. Such differences explain variations of the observed frequency ranges. For instance in Fig. 6(c), which is measured at the same current polarity as Fig. 6(a) but with the opposite field sweep direction, the frequencies are in the range of 0.74 to 0.84 GHz. Nevertheless, the data clearly demonstrate that in double vortex oscillators, dynamics can be excited for both current polarities and the resulting modes have distinct frequencies, which is consistent with the prediction of our model.

IV. SUMMARY

In summary, we have presented a spin-torque-based mechanism that quenches windmill-modes in double-vortex nanooscillators. The origin is frequency and phase adaption of the gyrotropic motions in the two disks, which results in a strong suppression of the gyration radius in one of the disks. Changing the sign of the product jC_1C_2 interchanges the roles of active and suppressed vortices. In particular, flipping the current sign at a fixed relative chirality combination provides, in agreement with our experimental data, an effective mode selection mechanism, which allows to deliberately choose between separated frequency bands of the oscillator.

*Present address: Institute of Ion Beam Physics and Materials Research, Helmholtz-Zentrum Dresden-Rossendorf e. V., D-01314 Dresden, Germany.

[1] S. A. Wolf, D. D. Awschalom, R. A. Buhrman, J. M. Daughton, S. von Molnár, M. L. Roukes, A. Y. Chtchelkanova, and D. M. Treger, Science **294**, 1488 (2001).

[2] S. I. Kiselev, J. C. Sankey, I. N. Krivorotov, N. C. Emley, R. J. Schoelkopf, R. A. Buhrman, and D. C. Ralph, Nature (London) **425**, 380 (2003).

[3] I. N. Krivorotov, N. C. Emley, J. C. Sankey, S. I. Kiselev, D. C. Ralph, and R. A. Buhrman, Science **307**, 228 (2005).

[4] F. B. Mancoff, N. D. Rizzo, B. N. Engel, and S. Tehrani, Nature (London) **437**, 393 (2005).

[5] S. Kaka, M. R. Pufall, W. H. Rippard, T. J. Silva, S. E. Russek, and J. A. Katine, Nature (London) **437**, 389 (2005).

[6] T. J. Silva and W. H. Rippard, J. Magn. Magn. Mater. **320**, 1260 (2007).

[7] A. M. Deac, A. Fukushima, H. Kubota, H. Maehara, Y. Suzuki, S. Yuasa, Y. Nagamine, K. Tsunekawa, D. D. Djayaprawira, and N. Watanabe, Nat. Phys. **4**, 803 (2008).

[8] J. C. Slonczewski, J. Magn. Magn. Mater. **159**, L1 (1996).

[9] L. Berger, Phys. Rev. B **54**, 9353 (1996).

[10] J. C. Slonczewski, J. Magn. Magn. Mater. **247**, 324 (2002).

[11] V. S. Pribiag, I. N. Krivorotov, G. D. Fuchs, P. M. Braganca, O. Ozatay, J. C. Sankey, D. C. Ralph, and R. A. Buhrman, Nat. Phys. **3**, 498 (2007).

[12] Y. Liu, H. He, and Z. Zhang, Appl. Phys. Lett. **91**, 242501 (2007).

[13] Y.-S. Choi, S.-K. Kim, K.-S. Lee, and Y.-S. Yu, Appl. Phys. Lett. **93**, 182508 (2008).

[14] Q. Mistral, M. van Kampen, G. Hrkac, J. V. Kim, T. Devolder, P. Crozat, C. Chappert, L. Lagae, and T. Schrefl, Phys. Rev. Lett. **100**, 257201 (2008).

[15] A. V. Khvalkovskiy, J. Grollier, A. Dussaux, K. A. Zvezdin, and V. Cros, Phys. Rev. B **80**, 140401(R) (2009).

[16] R. Lehndorff, D. E. Bürgler, S. Gliga, R. Hertel, P. Grünberg, C. M. Schneider, and Z. Celinski, Phys. Rev. B **80**, 054412 (2009).

[17] A. Dussaux, B. Georges, J. Grollier, V. Cros, A. V. Khvalkovskiy, A. Fukushima, M. Konoto, H. Kubota, K. Yakushiji, S. Yuasa, K. A. Zvezdin, K. Ando, and A. Fert, Nat. Commun. **1**, 8 (2010).

[18] X. W. Yu, V. S. Pribiag, Y. Acremann, A. A. Tulapurkar, T. Tyliszczak, K. W. Chou, B. Bräuer, Z.-P. Li, O. J. Lee, P. G. Gowtham, D. C. Ralph, R. A. Buhrman, and J. Stöhr, Phys. Rev. Lett. **106**, 167202 (2011).

[19] K. Y. Guslienko, G. R. Aranda, and J. Gonzalez, J. Phys.: Conf. Ser. **292**, 012006 (2011).

[20] N. Locatelli, V. V. Naletov, J. Grollier, G. de Loubens, V. Cros, C. Deranlot, C. Ulysse, G. Faini, O. Klein, and A. Fert, Appl. Phys. Lett. **98**, 062501 (2011).

[21] Y. B. Bazaliy, D. Olaosebikan, and B. A. Jones, J. Nanosci. Nanotechnol. **8**, 2891 (2008).

[22] A. A. Thiele, Phys. Rev. Lett. **30**, 230 (1973).

[23] B. A. Ivanov and C. E. Zaspel, Phys. Rev. Lett. **99**, 247208 (2007).

[24] E. Feldtkeller and H. Thomas, Phys. Kondens. Mater. **4**, 8 (1965).

[25] A. Wachowiak, J. Wiebe, M. Bode, O. Pietzsch, M. Morgenstern, and R. Wiesendanger, Science **298**, 577 (2002).

[26] A. V. Khvalkovskiy, J. Grollier, N. Locatelli, Ya. V. Gorbunov, K. A. Zvezdin, and V. Cros, Appl. Phys. Lett. **96**, 212507 (2010).

[27] K. Y. Guslienko, B. A. Ivanov, V. Novosad, Y. Otani, H. Shima, and K. Fukamichi, J. Appl. Phys. **91**, 8037 (2002).

[28] http://www.maplesoft.com/

[29] V. Sluka, A. Kákay, A. M. Deac, D. E. Bürgler, R. Hertel, and C. M. Schneider, J. Phys. D **44**, 384002 (2011).

[30] R. Lehndorff, D. E. Bürgler, C. M. Schneider, and Z. Celinski, Appl. Phys. Lett. **97**, 142503 (2010).